Metal nanoparticles entrapped in metal matrices

Dina Pinsky[1], Noam Ralbag[1], Ramesh Kumar Singh[2,3], Meirav Mann-Lahav[2], Gennady E. Shter[2], Gideon S. Grader*[2,3], Dario R. Dekel*[2,3] and David Avnir*[1]

[1]Institute of Chemistry and the Center for Nanoscience and Nanotechnology, The Hebrew University of Jerusalem, Jerusalem 9190401, Israel
[2]The Wolfson Department of Chemical Engineering, Technion–Israel Institute of Technology, Haifa 3200003, Israel
[3]The Nancy & Stephen Grand Technion Energy Program (GTEP), Technion – Israel Institute of Technology, Haifa 3200003, Israel

Supplementary Material

1. Additional experimental details

1.1 Chemicals

$AgNO_3$, $NaAuCl_4 \bullet 2H_2O$, $H_2PtCl_6 \bullet xH_2O$, $IrCl_3 \bullet xH_2O$, $NiCl_2 \bullet 6H_2O$ and K_2PtCl_4 were purchased from Alfa Aesar. $RhCl_3 \bullet xH_2O$ was purchased from Acros Organics. $NaBH_4$ and $PdCl_2$ were purchased from Strem Chemicals. H_3PO_2 50%, PVP K15 wt, trisodium citrate and Methyl Orange were purchased from Sigma Aldrich. NH_4OH 25%, HCl 37% and acetone were purchased from Bio Lab. NaOH 1 M was purchased from J.T.Baker. NaCl, $K_3Fe(CN)_6$ and $Na_2S_2O_3$ were purchased from BDH. Triple distilled water (TDW) with 18.3 MΩ/cm was taken from a Barnstead EasyPure UV apparatus.

1.2 Instrumentation and analytical methods

Scanning electron microscopy (SEM) characterizations were carried out with XHR (extra-high resolution) SEM Magellan 400L, coupled to electron dispersive spectroscopy (EDS) for element analysis. Transmission electron microscopy (TEM) characterizations were carried out with a ThermoFisher Tecnai F20 G2 STWIN instrument. Scanning transmission electron microscopy (STEM) characterizations were carried out with a ThermoFisher scientific Themis Z G3 instrument. Surface area of the composites was calculated using a linear fit to Brunauer - Emmett - Teller (BET) equation in the range of 0.05-0.25 P/P_0 of the adsorption isotherm determined with a Micromeritics ASAP 2020 instrument. Total pore volume of the composites was calculated using the values of the mass and the volume of the composite powder. The volume was measured through the compression of the powder into a marked syringe; the compressed powder was weighted to measure its mass. These two numbers provide the value of the bulk density. Along with the skeletal density, measured by pycnometer, the total pore volume of the powders was derived. Density was measured with a Micromeritics AccuPyc 1340 instrument using helium. Thermogravimetric analysis (TGA) was performed with a Mettler-Toledo TGA/SDTA 851e instrument under air in temperature range of 50-900 ^oC. X-ray diffraction (XRD) measurements were carried out with a D8

Bruker AXS diffractometer (CuKα1 (1.5418 A^{o}) with a step scan mode of 0.02 S-1). X-ray photoelectron spectroscopy (XPS) measurements were carried out with a Kratos Analytical Axis Ultra XPS/ESCA. Wavelength dispersive spectroscopy (WDS) was carried out with JEOL 8230 superprobe electron probe micro-analyzer (EPMA) with four wavelength-dispersive spectrometers for microanalysis (Beam conditions were set to 15 keV and 15 nA. All samples were analyzed for C, N, Br and Ag using silicate and oxide standards (SPI 53 minerals). Data were processed with a PRZ correction procedure). Catalytic activities of the Pt NPs were monitored using UV-Vis JASCO V630 spectrophotometer.

1.3 Synthesis of the NPs

Synthesis of Pt-NPs

Pt nanoparticles were prepared according to the procedure of ref[1] modified as follows: 329.0 mg of poly(vinylpyrrolidone), PVP, was dissolved in 40 mL triply distilled water (TDW) in a 100 mL beaker. 32.9 mg of H_2PtCl_6 (0.08 mmol) was added to the solution and stirred for 30 minutes. Then 30.3 mg of $NaBH_4$ (0.80 mmol) was dissolved in 2.5 mL of TDW and injected using a syringe to the PVP-Pt solution. The solution was stirred vigorously for another hour, during which it changed its color from yellow to dark brown-blackish. The NPs were precipitated by the addition of about 280 mL acetone, followed by centrifugation. The crude NPs were dried overnight and subsequently re-dispersed in 15 mL of TDW. The average particle size is 1.7 nm.

Synthesis of Au NPs

Au nanoparticles were prepared according to the procedure of ref[2] modified as follows: 289.4 mg of PVP was dissolved in 40 mL TDW. 28.94 mg of $NaAuCl_4$ (0.08 mmol) was added to the solution and stirred for 30 minutes. Then 30.3 mg of $NaBH_4$ (0.80 mmol) was dissolved in 2.5 mL of TDW and injected to the PVP-Au solution. The solution was stirred vigorously for another hour, during which it changed its color from yellow to dark red-wine. The NPs were precipitated by the addition of about 250 mL acetone, followed by centrifugation. The crude NPs were dried overnight and subsequently re-dispersed in 15 mL of TDW.

Synthesis of Ir NPs

Ir nanoparticles were prepared according to the procedure of ref[3] modified as follows: 15.6 mg of $IrCl_3$ (0.05 mmol) and 15 µL of HCl 37%, were dissolved in 20 mL TDW in a 50 mL round-bottomed flask. 111.1 mg of PVP was added to the solution and stirred for a few minutes. Then, the solution was heated to 60 ^{o}C and 94.57 mg of $NaBH_4$ (2.5 mmol) dissolved in 2.5 mL of TDW was injected to it. The solution was stirred for additional 4 hours, during which its color changed from yellow-orange to dark brown-blackish. The temperature was gradually decreased, first to 50 degrees after 2 hours, and afterwards to 30 degrees. The NPs were precipitated by the addition of about 120 mL acetone, followed by centrifugation. The crude NPs were dried overnight and subsequently re-dispersed in 9.6 mL of TDW.

Synthesis of Pd NPs

Pd nanoparticles were prepared according to the procedure of ref[4] modified as follows: 125.2 mg of PVP was dissolved in 25 mL TDW in a 100 mL beaker. 10.0 mg of $PdCl_2$ (0.056 mmol) and 80 µL of HCl 37% were added to the solution and stirred for 30 minutes. Then 60 mg of $NaBH_4$ (1.59 mmol) was dissolved in 2.5 mL of TDW and injected to the PVP-Pd solution. The solution was stirred vigorously for another hour during which the color changed from yellow to dark brown-blackish.

Nanoparticles sizes

Particle sizes were calculated by averaging the size of 100 particles, based on TEM images such as Fig. S1 (see Table 1, main text).

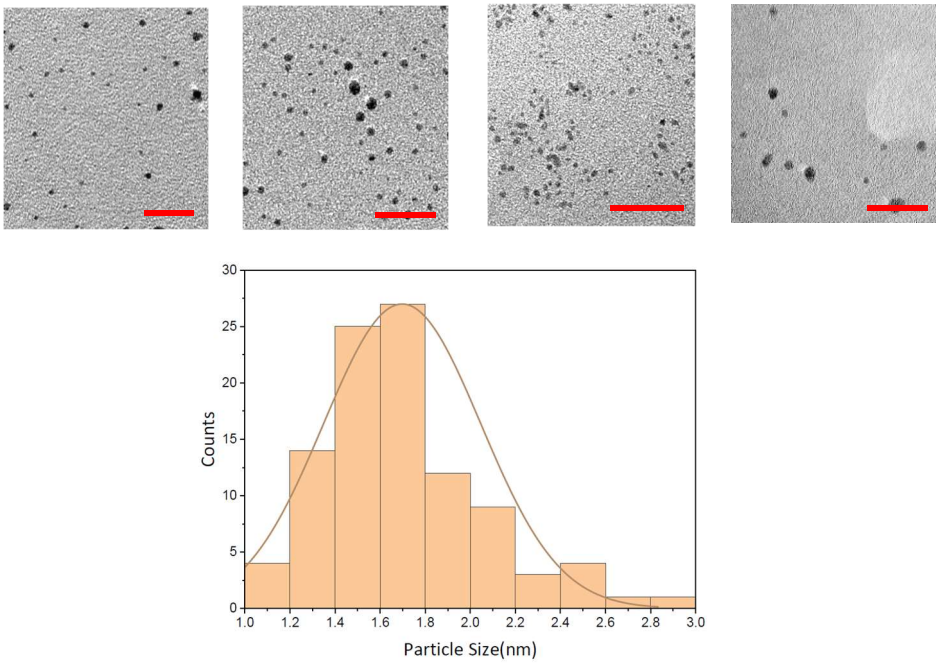

Figure S1. TEM images of Pt, Au, Ir and Pd NPs (left to right). Scale bars: 20 nm. Bottom: Typical particle size distribution, shown for the Ir NPs

1.4 Syntheses of all other M1-NP@M2 composites

1.4.1 Entrapment of Au-NPs within porous Ag - Type-A, denoted Au@Ag

6.0 mL of the prepared Au-NPs suspension (0.032 mmol of Au) was diluted to 10 mL with TDW, in a 25 mL vial. 314.9 mg of $AgNO_3$ (1.85 mmol) was added to the solution and stirred for a few minutes. 122 µL of H_3PO_2 (2.25 mmol) was added for the reduction of Ag. The solution was stirred overnight, after which the upper solution was transparent. The composite was then washed with 10 mL of NH_4OH for 15 minutes, followed by two washings of 10 mL of TDW for 10 minutes each. The powder was filtered with a

nylon filtering paper and dried in a desiccator under vacuum overnight. The filtrate was tested with NaCl for remains of unreduced Ag ions. The composite was grinded and mixed, weighted and kept in a vial.

1.4.2 Entrapment of Au-NPs within Ag foam - ***Type B****, denoted* ***Au@Ag-foam***

6.0 mL of the prepared Au-NPs suspension (0.032 mmol of Au) was diluted to 25 mL of TDW, in a 100 mL beaker. 314.9 mg of $AgNO_3$ (1.85 mmol) was added to the solution and stirred for a few minutes. 349.6 mg of $NaBH_4$ (9.24 mmol) was added for the reduction of Ag, that resulted in immediate formation of bubbles and emission of gas. The suspension was stirred for an hour, until the upper solution was transparent. The composite was then washed with 10 mL of NH_4OH for 15 minutes, followed by two washings of 10 mL of TDW for 10 minutes each. The powder was collected, dried and grinded, as described above.

1.4.3 In-situ generation of gold in porous Ag – ***Type C****, denoted* ***Au-grown@Ag***

200 mg (1.85 mmol) of porous Ag (see above, Type A, Pt@Ag) was added to 10 mL of TDW, in a 25 mL vial. 289.4 mg of PVP was added to the solution and stirred for 30 minutes. Afterwards, 62 µL of $NaAuCl_4$ solution 0.5 M (0.031 mmol) was added and the suspension was stirred for approximately an hour. The upper solution changed its color from yellow to colorless and the Ag powder was covered with a darker layer. The composite was then collected and clean as described above.

1.4.4 In-situ generation of gold in silver foam- ***Type D****, denoted* ***Au-grown@Ag-foam***

The composite was prepared similarly to Type C, using the Ag pure foam (described in Type B).

1.4.5 Entrapment of Ir-NPs within Rh foam - ***Type B****, denoted* ***Ir@Rh-foam***

3 mL of the prepared Ir-NPs suspension (0.016 mmol of Ir) were diluted to 12.5 mL of TDW, in a 50 mL beaker. 255.8 mg of $RhCl_3$ (0.97 mmol) was added to the solution and stirred for a few minutes. 550.4 mg of $NaBH_4$ (14.55 mmol) was added for the reduction of Rh and foam formation. Immediate formation of bubbles and emission of gas occurred. The composite was stirred for an hour, until the upper solution was transparent. The product was collected and cleaned as described above. Pure foam of rhodium was prepared for comparative purposes by the same procedure, but without the dopant.

1.4.6 Entrapment of Pd-NPs within Ni foam - ***Type B****, denoted* ***Pd@Ni-foam***

809.6 mg of $NiCl_2$ (3.41 mmol) was added to the Pd-NPs suspension (0.056 mmol of Pd) and stirred for a few minutes. 1286.2 mg of $NaBH_4$ (34.0 mmol) was added. Immediate formation of bubbles and emission of gas occurred. The composite was stirred for an hour, until the upper solution was transparent. The product was collected and cleaned as described above. Pure foam of nickel was prepared for comparative purposes by the same procedure, but without the dopant. The products contain NiO as well. The standard procedures in applying Ni-based catalysts include reduction of the metal-oxide immediately prior to use - this step was beyond the scope of this study. The synthesis was also carried

out with the diffusion of Ar gas into the solution. However, since this approach didn't achieve significant decrease in the oxidation of the matrix, it will not be presented.

1.4.7 In-situ generation of palladium in Ni fibers - denoted ***Pd-grown@Ni***

100 mg of pure Ni fibers (1.70 mmol) prepared from NiO fibers according to ref[5] and supplied by the authors was added to 5 mL of TDW in a 25 mL vial. A mechanical stirrer was used to stir the solution. Afterwards, 0.5 mL of $PdCl_2$ solution, 0.03 mmol (20.4 mg $PdCl_2$ +20 µL HCl 37% in 2 mL of TDW) was added and the composite was stirred for approximately a half an hour. The upper solution changed its color from yellow to colorless. The composite was then washed with two portions of 10 mL of TDW for 10 minutes each. Afterwards, the powder was filtered, dried and grinded, and kept in a vial.

2. Additional results and discussion

2.1 The synthesis of the Pt NPs

The specific synthesis of the Pt NPs prior to their entrapment in silver (types A,B) is a crucial step because the choice of the stabilizing agent for the Pt NPs has a significant effect on the success of the later steps in the process. Poly(vinylpyrrolidone) (PVP) was found to be most suitable for that purpose[6,7], yielding NPs of <10 nm size[8], keeping the dispersion stable for long periods[9]. These were synthesized from hexachloroplatinic acid using sodium borohydride as the reducing agent[1] according to:

$$2Pt^{4+}{}_{(aq)} + PVP_{(aq)} + BH_4^-{}_{(aq)} + 3H_2O_{(l)} \Rightarrow 2Pt\text{-}PVP_{(s)} + B(OH)_{3(aq)} + 7H^+{}_{(aq)}.$$

Prior to their entrapment, the NPs (average size of 1.7 nm. See Table 1 and Fig. S1, for these NPs and for all other NPs described below) were cleaned from the PVP (by precipitation in acetone and re-dispersion in water), in order to avoid blocking of the activity of the Pt NPs. The loading of the NPs in the final composite was another parameter to be considered. On the one hand, the amount of the dopant has to be sufficient for applications such as catalysis, but on the other hand, it has to be well dispersed in the composite with no significant aggregation and phase separation.

2.2 Additional results for the Pt-in-Ag systems

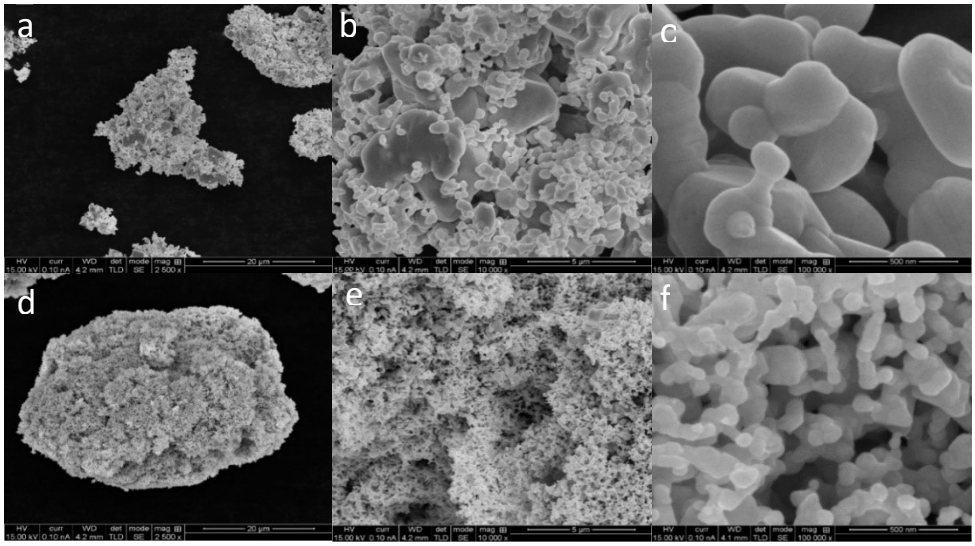

Figure S2. XHR-SEM images of Ag blanks: (a), (b), (c) and (d), (e), (f) are different magnification images of aggregated and foam matrices, respectively.

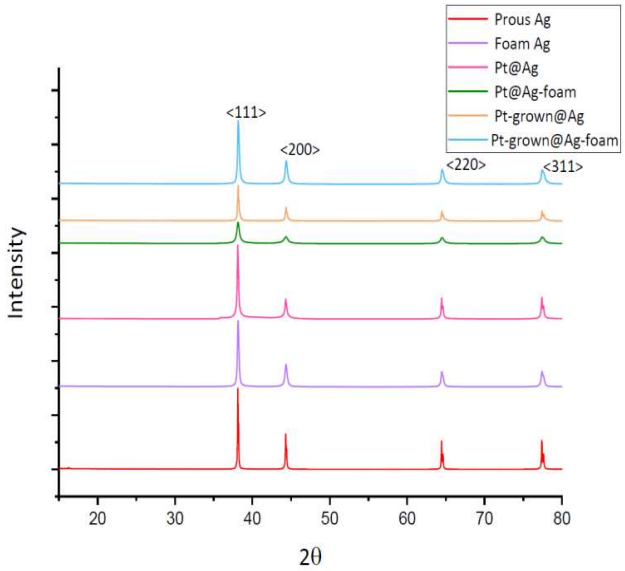

Figure S3. XRD spectra of the silver matrix in the different composites. Ag crystal facets are indicated

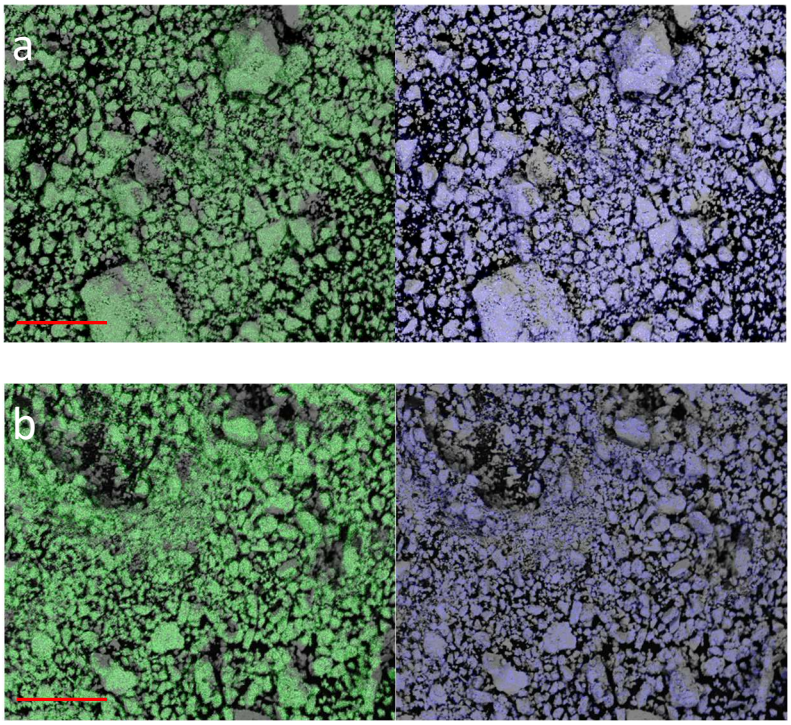

Figure S4. EDS maps of platinum within silver composites of (a) Pt@Ag-foam and (b) Pt-grown@Ag-foam. Green and blue represent areas with Ag and Pt, respectively. Scale bars: 0.2 mm.

2.3 Material characterizations of all other metal-NPs@metal systems

In this section we show that the procedures developed for Pt in Ag are in fact general, and can be applied to other pairs of metals – gold within silver, iridium within rhodium and palladium within nickel. Since many of the features of these additional pairs are similar to those described above, we shall briefly present the representative observations and provide most of the accompanying figures in the Supplementary Material.

The gold within silver sets of metals was successfully synthesized in all the methodologies developed above, namely: Au@Ag, Au@Ag-foam, Au-grown@Ag, and Au-grown@Ag-foam. SEM images of Au@Ag, Au@Ag-foam (types A and B) are seen in Fig. S6. The structures of the gold-silver matrices resemble the matrices seen for the entrapped platinum within silver composites: it is hierarchical, composed of aggregates that are built from smaller crystals. The differences between the foam and the porous matrices are clear as was the case for the Pt-Ag composites. Next, the *in-situ* grown gold within silver composites, Au-grown@Ag and Au-grown@Ag-foam (types C and D) were examined and are shown in Fig. S7: Au-grown@Ag is composed of larger aggregates compared to the Au-grown@Ag-foam net-like highly porous structure, and in both composites, cavities that are generated during the reduction of the Au cation by the Ag matrix are seen. All gold within silver composites were also examined with EDS coupled to the SEM (Fig. S8) and these local elemental analyses revealed again that in all types there is no

phase separation. Next, the composites were characterized by XRD for Ag crystal size determination, and surface areas were determined using nitrogen physisorption and BET theory - the results are collected in Table S1. It can be seen again that the crystal sizes of Ag in the foam materials are smaller compared to the regular porous Ag, and that the Ag crystal sizes in the entrapped composites (Au@Ag and Au@Ag-foam) are smaller than those of the pure silver matrices; the explanation of this and the other trends in Table S1 follows the previously used arguments, and will not be repeated here. A difference is however seen for the Au-grown@Ag-foam, which shows a *decrease* in surface area compared to the pure Ag foam, contrary to what we have seen above for the Pt-grown@Ag-foam. The possible interpretation is that since Au is a better wetting metal compared to Pt, Au blocks more efficiently the micropores in this case. Overall, the changes of the surface area in the grown Au composites are more moderate compared to the grown Pt composites, probably since the reduction of the Pt^{4+} ions require the oxidation of 4 Ag atoms from the matrix, while the metallic gold is formed from Au^{3+}, requiring 3 Ag atoms for the reduction. TEM images of the gold in silver systems are provided in Fig.'s S9 and S10. Contrary to the platinum within silver Types A and B, the distinct separation between the NPs and the matrix is not seen here (Fig. S9). This may be due to the fact that contrary to Pt, Ag is known to wet Au, especially when reducing its size[10].

Due to their higher surface areas, we focused on additional metal foam composites, Ir@Rh-foam and Pd@Ni-foam, all four metals of which are also well-known metallic catalysts. They showed similar material characteristics to the composites described above, exhibiting the typical porous hierarchal structure of the foams described so far – see Fig.'s S11 and S12 for Ir@Rh-foam, and Fig.'s S13 and S14(a) for Pd@Ni-foam. The Pd NPs are not observed by SEM due to instrumental limitations in the presence of the magnetic Ni, but were detected as well-dispersed by EDS (Fig. S14(a)). These two foams also comprise examples of syntheses that are accompanied by surface oxidations (which, in catalysis, are removed if needed by hydrogen reduction prior to use). Thus, XPS measurements indicated the formation rhodium oxide - about 55% - on the surface of the matrix. After etching with an Ar^+ to a depth of ~60 nm, the oxidized Rh decreases to about 15%, indicating that most of the matrix is metallic. Similar observations were obtained for the Ir NPs: The surface is oxidized to about 40%, but inside of the matrix this value drops to only 5%. This oxidation is particularly known for Ni, for which NiO coating readily forms. Again, etching of the surface of Pd@Ni-foam using Ar^+ ion beam showed by etching XPS a transition to the metal, below that coating.

It turns out, however, that the decoration of Ni with NiO is known in the literature to be beneficial for the HOR[11–14]. In order to test the applicability of the entrapment method for such cases where the oxide decoration is useful, and at the same time to show that this methodology is applicable also for other types of porous matrices, we doped a porous mat of Ni fibers with Pd (a HOR catalyst as well[15]). The Ni fibers, about 250 nm in diameter and 1 micron long with a surface area 4.5 m^2/g (Fig. S5(a),(b)) were synthesized from NiO mats as described in detail in ref[5] and generously provided by the authors of that report. The doping with Pd was of the type-C approach, that is, the matrix Ni was used as a reducing agent for the growing Pd according to:

$$Ni_{(s)} + Pd^{2+}_{(aq)} \Rightarrow Pd_{(s)} + Ni^{2+}_{(aq)}.$$

The resulting Pd-grown@Ni-fibers and the Pd distribution are shown in Fig's 11 and S14(b). The Pd grown composite preserves the fiber structure of the matrix (Fig. 11(e)); however, its surface is less porous compared to the blank due to the formation of Pd islands covering the fibers (Fig. 11(f)). EDS analysis, Fig. S14(b), shows that the Pd counts are somewhat more heterogeneous than other distributions we have seen above, and partial surface oxidation of the Ni is seen as well (Fig. S14(c)).

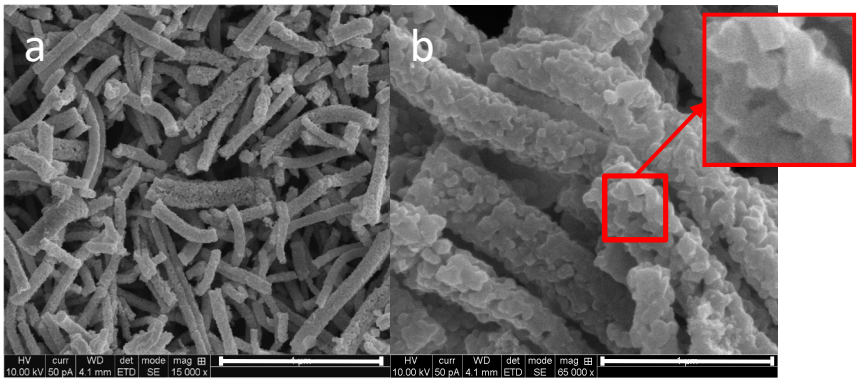

Figure S5. XHR-SEM images of Ni fibers matrix (a,b). Close-up of the surface morphology can be seen in the squares. Bars: (a) – 4 μm, (b) – 1 μm.

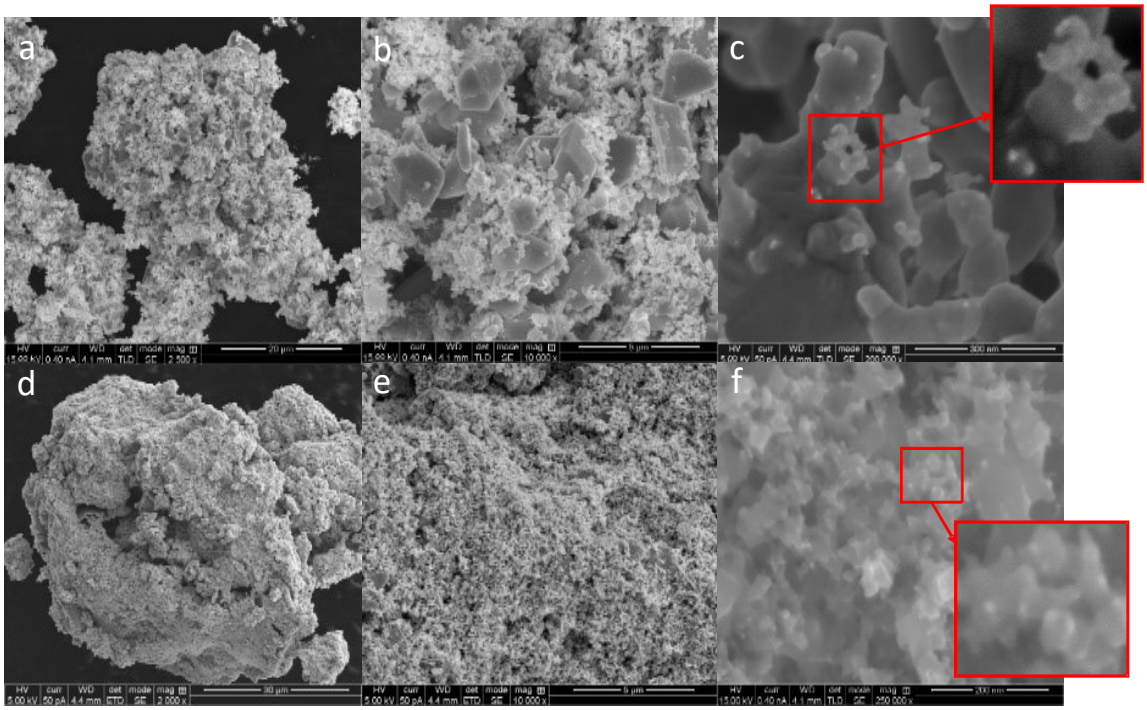

Figure S6. XHR-SEM images of entrapped gold within silver composites: (a),(b),(c) and (d),(e),(f) are different magnifications of Au@Ag and Au@Ag-foam composites, respectively. Au-NPs of approximately 2 nm can be seen in the red squares.

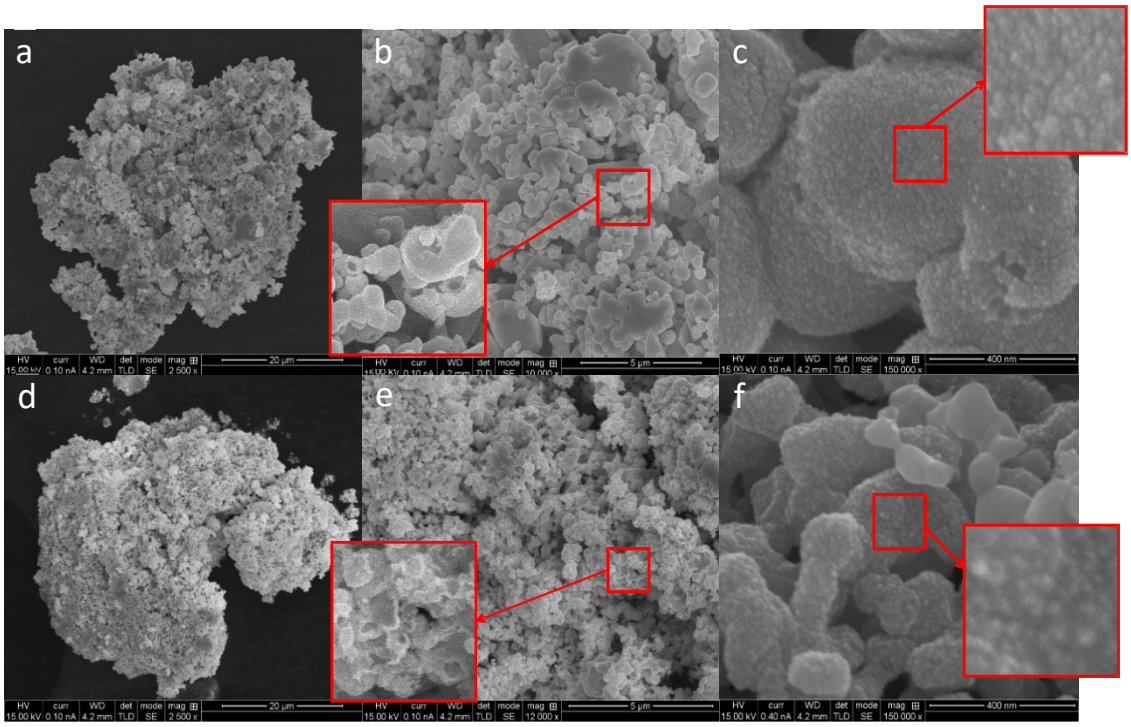

Figure S7. XHR-SEM images of grown gold within silver composites: (a),(b),(c) and (d),(e),(f) are different magnifications of Au-grown@Ag and Au-grown@Ag-foam composites, respectively. Cavities in the surface are apparent in the squares in (b) and (e). Au particles and islands can be seen on the surface in the red squares in (c) and (f).

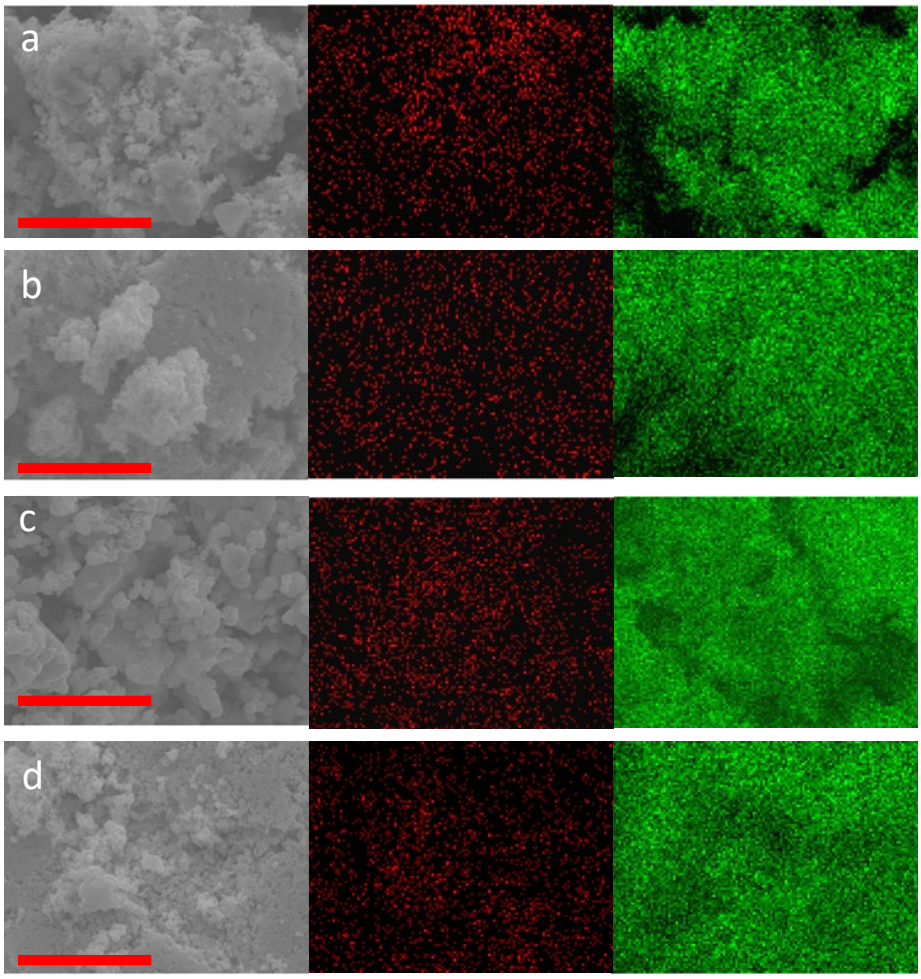

Figure S8. HR-SEM images and EDS elemental maps of gold within silver composites: (a),(b),(c),(d) represent Au@Ag, Au@Ag-foam, Au-grown@Ag and Au-grown@Ag-foam composites, respectively. Red and green are the detected Au and Ag, respectively. Bars: 6 μm.

Table S1. Crystal sizes and surface areas of gold within silver composites

Composite	Crystal Size (nm)	Surface Area (m^2/g)
Pure porous Ag	93.4	0.36
Pure Ag foam	42.3	2.36
Au@Ag	80.2	1.94
Au@Ag-foam	27.9	8.31
Au-grown@Ag	72.9	0.38
Au-grown@Ag-foam	42.8	1.97

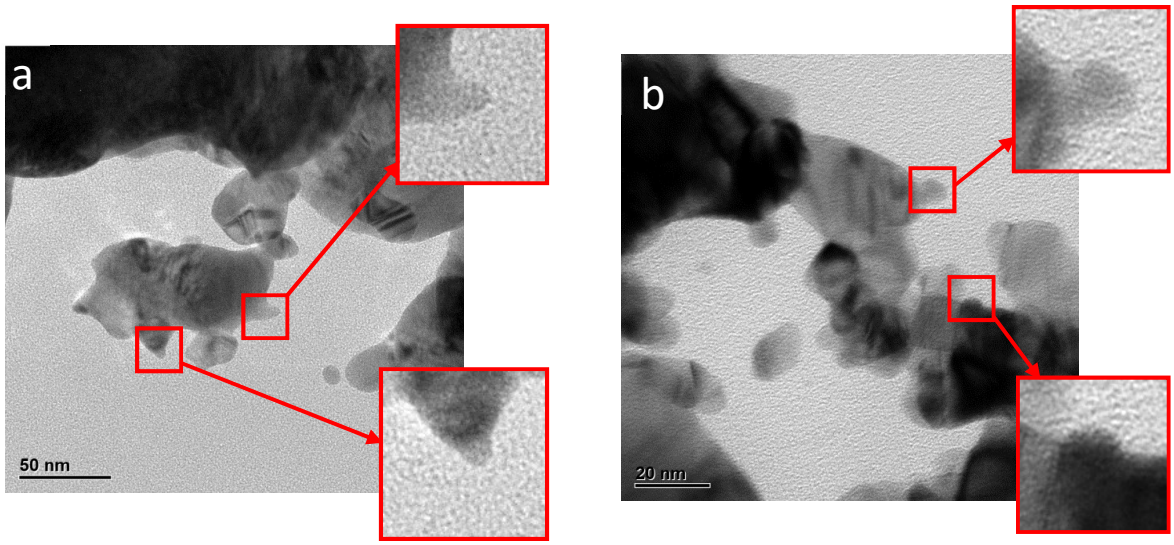

Figure S9. HR-TEM images of entrapped gold within silver composites: (a)Au@Ag (b) Au@Ag-foam. Pt NPs can be seen in red squares.

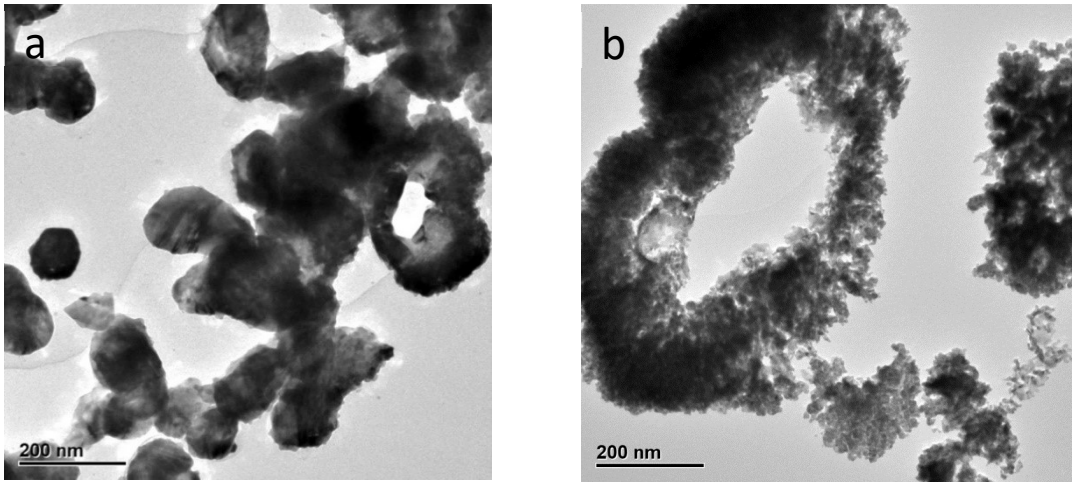

Figure S10. HR-TEM images of grown gold within silver composites: (a) Au-grown@Ag (b) Au-grown@Ag-foam.

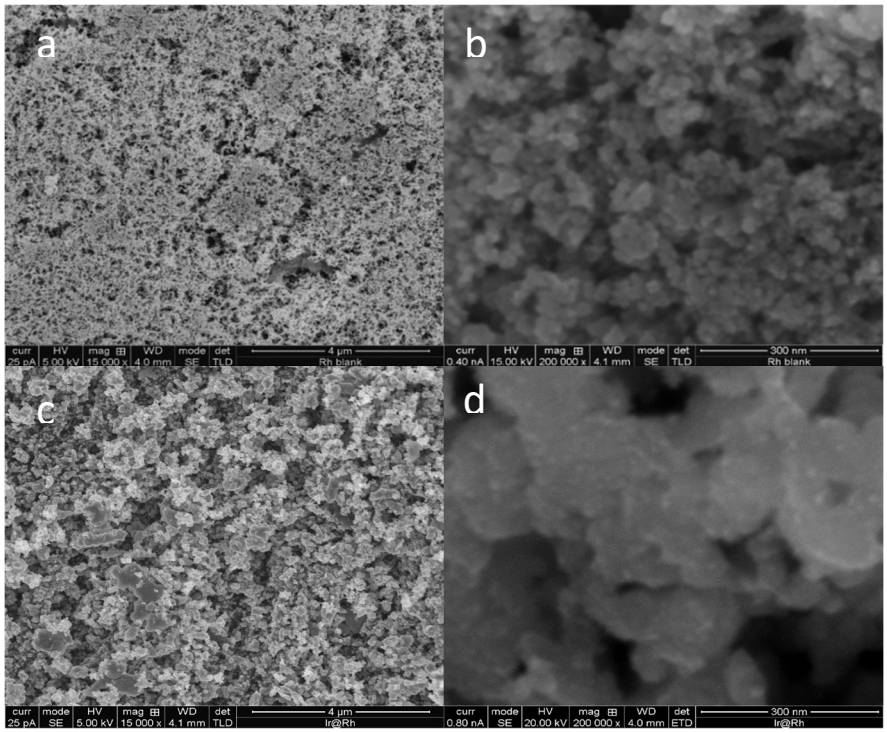

Figure S11. XHR-SEM images of pure Rh foam matrix (a and b) and of Ir@Rh-foam composite (c and d).

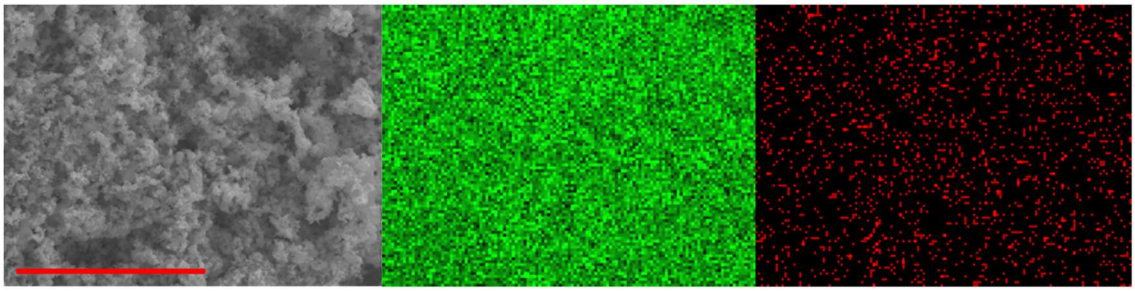

Figure S12. HR-SEM images and EDS elemental maps and of Ir@Rh-foam composite. Red and green: Ir and Rh; scale bar: 5 µm

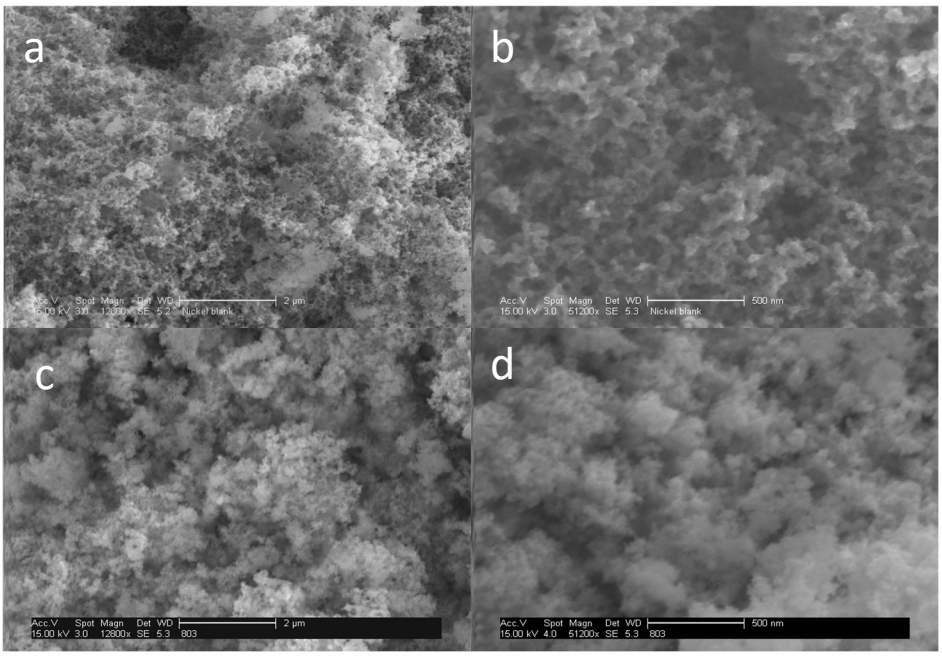

Figure S13. HR-SEM images of pure Ni foam matrix (a, b) and of the Pd@Ni-foam composite (c, d).

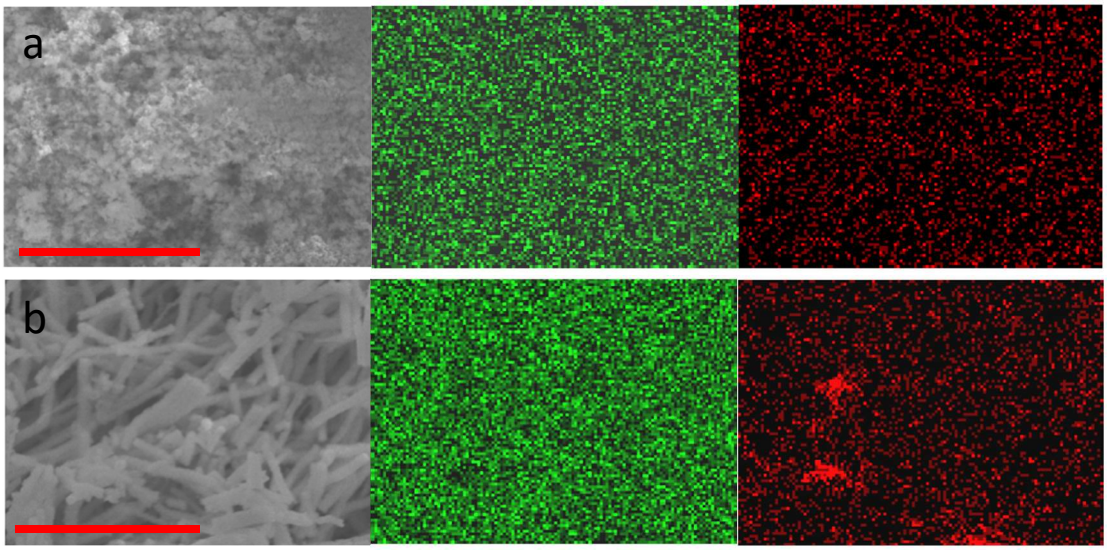

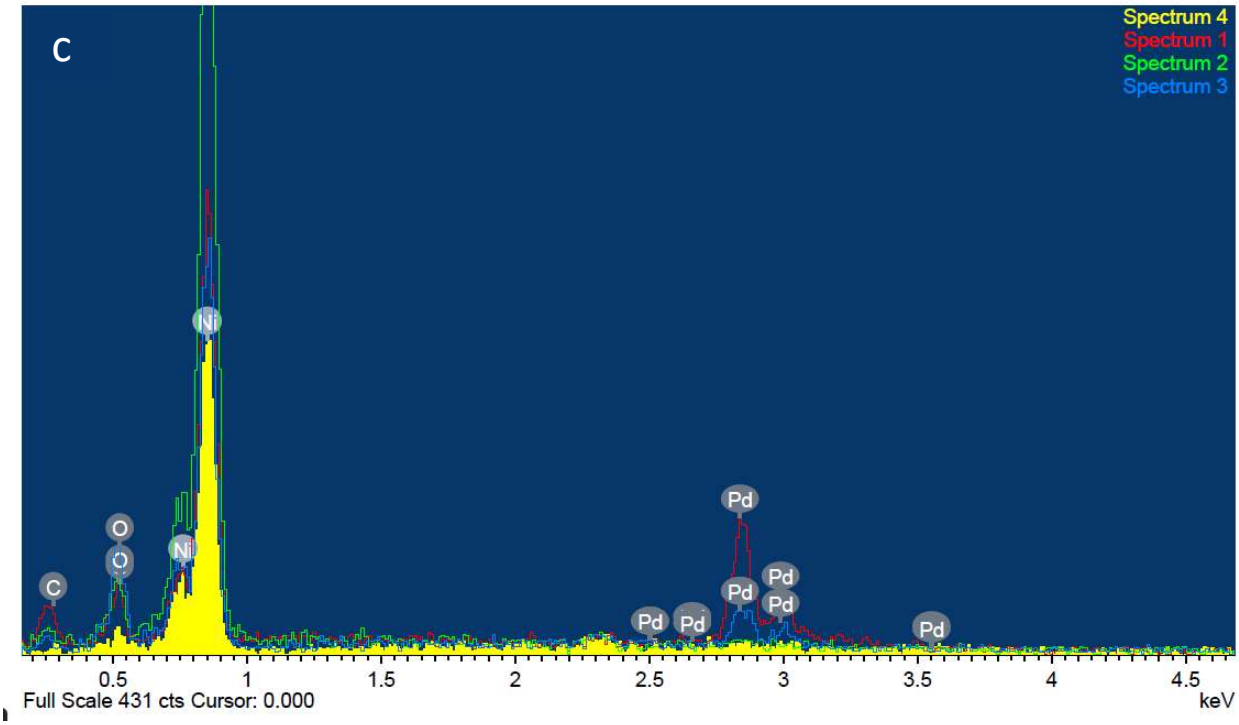

Figure S14. HR-SEM images and EDS local elemental maps of palladium within nickel composites: (a) and (b) represent Pd@Ni-foam and Pd-grown@Ni-fiber composites, respectively. Red and green colors are the detected Ni and Pd, respectively. Scale bars are of 5 μm. (c) Local elemental EDS spectrum of Pd-grown@Ni-fiber, showing the presence of some NiO.

2.4 Additional results for the catalysis section

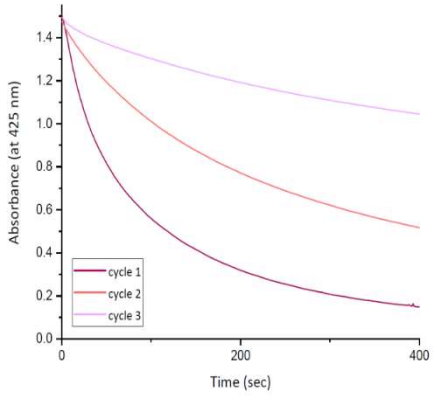

Figure S15. Recycling test on Pt@Ag composite in the hexacyanoferrate reduction.

References

(1) Bedia, J.; Lemus, J.; Calvo, L.; Rodriguez, J. J.; Gilarranz, M. A. Effect of the Operating Conditions on the Colloidal and Microemulsion Synthesis of Pt in Aqueous Phase. *Colloids Surfaces A Physicochem. Eng. Asp.* **2017**, *525* (February), 77–84.

(2) Tsunoyama, H.; Sakurai, H.; Ichikuni, N.; Negishi, Y.; Tsukuda, T. Colloidal Gold Nanoparticles as Catalyst for Carbon-Carbon Bond Formation: Application to Aerobic Homocoupling of Phenylboronic Acid in Water. *Langmuir* **2004**, *20* (26), 11293–11296.

(3) Sharif, M. J.; Maity, P.; Yamazoe, S.; Tsukuda, T. Selective Hydrogenation of Nitroaromatics by Colloidal Iridium Nanoparticles. *Chem. Lett.* **2013**, *42* (9), 1023–1025.

(4) Zhao, Y.; Baeza, J. A.; Koteswara Rao, N.; Calvo, L.; Gilarranz, M. A.; Li, Y. D.; Lefferts, L. Unsupported PVA- and PVP-Stabilized Pd Nanoparticles as Catalyst for Nitrite Hydrogenation in Aqueous Phase. *J. Catal.* **2014**, *318*, 162–169.

(5) Landman, A.; Hadash, S.; Shter, G. E.; Dotan, H.; Rothschild, A.; Gideon, S. High Performance Core-Shell Ni / Ni (OH) 2 Electrospun Nanofiber Anodes for Decoupled Water Splitting. 1–60.

(6) Saldias, C.; Bonardd, S.; Quezada, C.; Radic, D.; Leiva, A. The Role of Polymers in the Synthesis of Noble Metal Nanoparticles: A Review. *J. Nanosci. Nanotechnol.* **2017**, *17* (1), 87–114.

(7) Koczkur, K. M.; Mourdikoudis, S.; Polavarapu, L.; Skrabalak, S. E. Polyvinylpyrrolidone (PVP) in Nanoparticle Synthesis. *Dalt. Trans.* **2015**, *44* (41), 17883–17905.

(8) Hei, H.; Wang, R.; Liu, X.; He, L.; Zhang, G. Controlled Synthesis and Characterization of Nobel Metal Nanoparticles. *Soft Nanosci. Lett.* **2012**, *02* (03), 34–40.

(9) Bonet, F.; Delmas, V.; Grugeon, S.; Herrera Urbina, R.; Silvert, P. Y.; Tekaia-Elhsissen, K. Synthesis of Monodisperse Au, Pt, Pd, Ru and Ir Nanoparticles in Ethylene Glycol. *Nanostructured Mater.* **1999**, *11* (8), 1277–1284.

(10) Grouchko, M.; Roitman, P.; Zhu, X.; Popov, I.; Kamyshny, A.; Su, H.; Magdassi, S. Merging of Metal Nanoparticles Driven by Selective Wettability of Silver Nanostructures. *Nat. Commun.* **2014**, *5*, 1–6.

(11) Pan, Y.; Hu, G.; Lu, J.; Xiao, L.; Zhuang, L. Ni(OH)2-Ni/C for Hydrogen Oxidation Reaction in Alkaline Media. *J. Energy Chem.* **2019**, *29*, 111–115.

(12) Campos-Roldán, C. A.; Calvillo, L.; Boaro, M.; De Guadalupe González-Huerta, R.; Granozzi, G.; Alonso-Vante, N. NiO-Ni/CNT as an Efficient Hydrogen Electrode Catalyst for a Unitized Regenerative Alkaline Microfluidic Cell. *ACS Appl. Energy Mater.* **2020**, *3* (5), 4746–4755.

(13) Yang, Y.; Sun, X.; Han, G.; Liu, X.; Zhang, X.; Sun, Y.; Zhang, M.; Cao, Z.; Sun, Y. Enhanced Electrocatalytic Hydrogen Oxidation on Ni/NiO/C Derived from a Nickel-Based Metal–Organic Framework. *Angew. Chemie - Int. Ed.* **2019**, *58* (31), 10644–10649.

(14) Biemolt, J.; Douglin, J. C.; Singh, R. K.; Davydova, E. S.; Yan, N.; Rothenberg, G.; Dekel, D. R. An Anion-Exchange Membrane Fuel Cell Containing Only Abundant and Affordable Materials. *Energy Technol.* **2021**, *2000909*.

(15) Alesker, M.; Page, M.; Shviro, M.; Paska, Y.; Gershinsky, G.; Dekel, D. R.; Zitoun, D. Palladium/Nickel Bifunctional Electrocatalyst for Hydrogen Oxidation Reaction in Alkaline Membrane Fuel Cell. *J. Power Sources* **2016**, *304*, 332–339.